Lab on a Chip

PAPER

View Article Online
View Journal

Cite this: DOI: 10.1039/d0lc01063d

A microfluidic cathodic photoelectrochemical biosensor chip for the targeted detection of cytokeratin 19 fragments 21-1†

Jinhui Feng,[a] Tingting Wu,[a] Qian Cheng,[a] Hongmin Ma,[a] Xiang Ren,*[a] Xueying Wang,[a] Jin Yong Lee,[b] Qin Wei*[a] and Huangxian Ju*[a]

A microfluidic chip integrated with a microelectrode and a cathodic photoelectrochemical (PEC) biosensor for the ultrasensitive detection of non-small cell lung cancer cytokeratin fragments based on a signal amplification strategy was designed. The mechanism for signal amplification is developed based on the p–n junction of AgI/$Bi_2Ga_4O_9$, with dissolved O_2 as an electron acceptor to produce the superoxide anion radical ($^{\bullet}O_2^-$) as the working microelectrode. By combining this with a novel superoxide-dismutase-loaded honeycomb manganese oxide nanostructure (SOD@hMnO_2) as the co-catalyst signal amplification label, $^{\bullet}O_2^-$ can be catalyzed by SOD *via* a disproportionation reaction to produce O_2 and H_2O_2; then, hMnO_2 is able to trigger the decomposition of H_2O_2 to generate O_2 and H_2O. Therefore, the increased O_2 promotes the separation of electron–hole pairs *via* consuming more electrons, leading to an effective enhancement of the cathodic PEC behavior. Under optimum conditions, with the cytokeratin 19 fragments 21-1 (CYFRA 21-1) as the targeted detection objects, the microfluidic cathodic PEC biosensor chip exhibited excellent linearity from 0.1 pg mL^{-1} to 100 ng mL^{-1}, with a detection limit of 0.026 pg mL^{-1} (S/N = 3). The exciting thing that this work offers is a new strategy for the detection of other important cancer biomarkers for disease diagnosis and prognosis.

Received 23rd October 2020,
Accepted 23rd November 2020

DOI: 10.1039/d0lc01063d

rsc.li/loc

Introduction

The portability of traditional photoelectrochemical (PEC) biosensors is greatly limited by miniaturization and automation.[1,2] Surprisingly, microfluidic chip integrated microelectrodes with high portability, strong automation, low sample consumption, and good disposability provide good techniques to overcome the limitations.[3–6] In addition, the cathodic PEC biosensor, one of the latest directions, represents a newly developed eye-catching tool for sensitive biomolecule detection by complementary advantages of PEC bioanalysis and photocathode. Compared with photoanode mode, the cathodic PEC biosensor has great capability to resist the interference of reductive substances because of it is more likely to react with the electron acceptors (*e.g.*, dissolved O_2) than the electron donors (*e.g.*, ascorbic acid) in an electrolyte.[7–9] Despite groundbreaking advances in biosensors, the innovative and effective signaling amplifying strategy is still highly needed to promote broader application in clinical diagnosis. For this purpose, the microfluidic cathodic PEC biosensor based on facilitating the separation of electron–hole pair by consuming electron acceptor of dissolved O_2 is applied.

High-performance cathode PEC bioanalysis is inseparable from excellent p-type semiconductor materials, such as metal oxides (*e.g.* Cu_2O,[10,11] CuO,[12] and NiO (ref. 13 and 14)); Ag-based materials (*e.g.* Ag_2S (ref. 15) and AgI (ref. 16)); and various heterostructures.[17] Among them, AgI, as a typical p-type semiconductor, has attracted much attention because of its good visible light response with a suitable narrow band gap.[7,18] However, the separation of photogenerated carriers is suppressed by the high recombination rate of individual AgI, but the construction of a p–n junction at the interface between two semiconductors offers an effective method to enhance visible-light absorption and charge carrier separation.[19,20] Inspired by this, the n-type mullite-type orthorhombic $Bi_2Ga_4O_9$ with a good photocatalyst could be combined with p-type AgI to form a p–n junction at the interface of AgI/$Bi_2Ga_4O_9$. In general, a strong internal electric field is created *via* band bending, due to the large difference of Fermi level (E_f) at the interface of the p–n junction,

[a] *Collaborative Innovation Center for Green Chemical Manufacturing and Accurate Detection, Key Laboratory of Interfacial Reaction & Sensing Analysis in Universities of Shandong, School of Chemistry and Chemical Engineering, University of Jinan, Jinan 250022, PR China. E-mail: chem_renx@163.com, sdjndxwq@163.com, hxju@nju.edu.cn*

[b] *Department of Chemistry, Sungkyunkwan University, Suwon, 16419, Republic of Korea*

† Electronic supplementary information (ESI) available. See DOI: 10.1039/d0lc01063d

resulting in improving the separation and transfer of photogenerated charge carriers effectively and further enhancing photocurrent conversion efficiency.[21–23] Under visible light irradiation, the crucial role of the p–n junction for enhancing the PEC cathode response was revealed by using dissolved O_2 as the electron acceptor to improve the superoxide radical ($^{\bullet}O_2^-$) generation rate and increase the separation efficiency of the electron–hole pairs.

To further achieve amplification of the detectable signal, it is critical to eliminate $^{\bullet}O_2^-$ and increase the dissolved O_2. Superoxide dismutase (SOD), a natural scavenger of oxygen free radicals, has attracted widespread attention in protection mechanisms against oxidative damage from reactive oxygen species by catalyzing the dismutation of $^{\bullet}O_2^-$ to O_2 and H_2O_2.[24,25] Unfortunately, the presence of H_2O_2 limits the maximum extent of the reaction. Honeycomb MnO_2 ($hMnO_2$) nanostructures as a catalyst could be able to trigger the decomposition of H_2O_2 into H_2O and O_2,[26,27] so as to increase the electron acceptor of dissolved O_2 to enhance the cathodic PEC signals. Moreover, $hMnO_2$ possesses the excellent merits of low toxicity, easy preparation, high loading capacity, and low-cost and has exhibited increasing potential for applications in biosensing. To better perform the functions of SOD with $hMnO_2$, a collaborative amplification strategy, in which SOD is loaded onto the surface of a $hMnO_2$ (SOD@$hMnO_2$) nanostructure is proposed.

Herein, a highly efficient microfluidic cathodic PEC biosensor system was developed for biomarker detection by applying p–n AgI/$Bi_2Ga_4O_9$ as the sensing substrate and SOD@$hMnO_2$ as the signal amplification label. In addition, the satisfying practicability and accuracy of the prepared cathodic PEC biosensor was well proven using the real antigen target of cytokeratin 19 fragments 21-1 (CYFRA 21-1), a reliable biomarker of non-small cell lung cancer. To improve the interfacial specificity of the CYFRA 21-1 antigen, primary antibodies (Ab_1) were directly incubated on the large surface of AgI/$Bi_2Ga_4O_9$ modified with thioglycolic acid (TGA) through activating –COOH by EDC/NHS. After incubating the detection antibody (Ab_2) on the SOD@$hMnO_2$ (SOD@$hMnO_2$–Ab_2) bioconjugate, a sandwich-type immunocomplex was prepared. What is more, the p–n AgI/$Bi_2Ga_4O_9$ increases the generation rate of $^{\bullet}O_2^-$, then the $^{\bullet}O_2^-$ can be catalyzed by SOD *via* a disproportionation reaction, producing O_2 and H_2O_2; the $hMnO_2$ can further degrade H_2O_2 to generate O_2 and H_2O; the more O_2 produced increases the content of dissolved O_2 captured by more electrons, which promotes the separation of electron–hole (e^-/h^+) pairs, leading to the amplification of the cathodic PEC signal in the microfluidic chip.

Experimental section

Preparation of the microfluidic chip

Firstly, ITO was cut into 6 cm × 5 cm slices for the fabrication of wet etching on the ITO slices according to the published work as shown in Fig. 1A. After that, the p–n AgI/$Bi_2Ga_4O_9$ was modified on the working microelectrode (WE) of the ITO

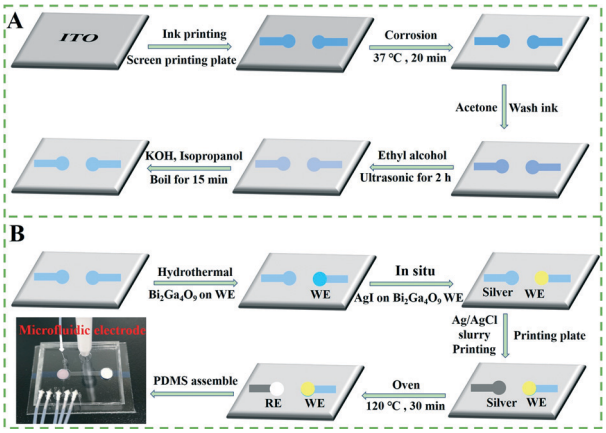

Fig. 1 Wet etching on ITO (A), and the preparation of the microfluidic working microelectrode (WE) and reference microelectrode (RE) (B).

substrate by the electrostatic self-assembly process and silver/silver chloride (Ag/AgCl) conductive ink was printed on the reference microelectrode (RE) of the ITO substrate through the silk-screen mode, then dried at 120 °C for 30 min in Fig. 1B. In detail, the $Bi_2Ga_4O_9$ nanostructures were synthesized by a corrosion and hydrothermal method based on previous reports with a slight modification.[28,29] 0.033 M Ga_2O_3 in 100 mM NaOH aqueous solution was added in a 100 mL Teflon-lined stainless autoclave, which was kept at 180 °C for 48 h. After cooling, 0.580 g of $Bi(NO_3)_3{\cdot}5H_2O$ was added to the above solution and stirred for 60 min, then the cleaned and etched ITO WE was added to the 100 mL Teflon-lined stainless autoclave which was kept at 200 °C for another 10 h. After the reaction, a pale-yellow precipitate on the WE was acquired after washing with ultrapure water. The acquired precipitate was further added to 4 M HNO_3 for 20 s and then washed with ultrapure water. Finally, the prepared $Bi_2Ga_4O_9$ nanostructures on the WE were gained by drying at 60 °C for 2 h. Then, the $Bi_2Ga_4O_9$ nanostructures were sequentially immersed into 10 mL of 0.05 mol L^{-1} KI and 0.05 mol L^{-1} $AgNO_3$ aqueous solution for 10 min in the dark, respectively, six times and then washed with ultrapure water and dried at room temperature. Then, 8 μL of 10 mM TGA solution was dropped onto the surface of p–n AgI/$Bi_2Ga_4O_9$ and dried at room temperature. After washing with ultrapure water, the p–n AgI/$Bi_2Ga_4O_9$ modified with carboxyl functionalization was obtained. The other details are in the ESI.†

Preparation of SOD@$hMnO_2$–Ab_2

As shown in Fig. 2A, the honeycomb MnO_2 ($hMnO_2$) nanostructures were synthesized by a redox reaction method based on previous reports (detailed in ESI†). The prepared 0.2 g $hMnO_2$ was dispersed in 20 mL of ethanol containing 0.3 mL of APTES and heated at 70 °C for 1.5 h under constant stirring to gain amino functionalized $hMnO_2$ ($hMnO_2$–NH_2). Then, $hMnO_2$–NH_2 (2 mL, 3 mg mL^{-1}) was mixed with glutaraldehyde (GA) (1 mL, 2.5%) and stirred for 2 h at room temperature to activate $hMnO_2$–NH_2. After washing with

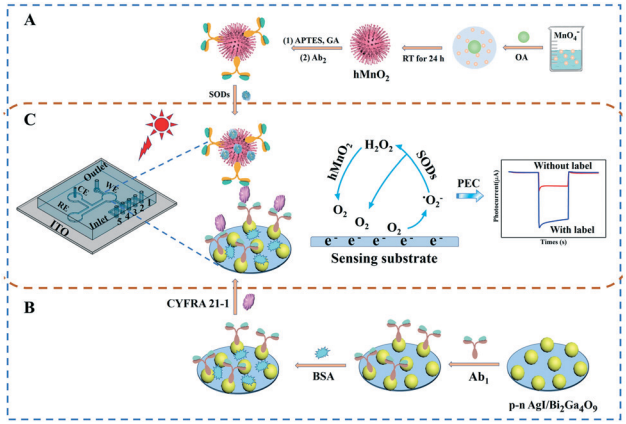

Fig. 2 The preparation process of the SOD@hMnO$_2$–Ab$_2$ bioconjugate (A) and the developed microfluidic PEC biosensor for CYFRA 21-1 detection ((B) and (C)).

phosphate buffer (pH 7.0), the activated hMnO$_2$–NH$_2$ was re-dispersed in PBS and then successively incubated with Ab$_2$ solution (1 mL, 10 μg mL^{-1}) and SOD solution (400 μL, 0.5 mg mL^{-1}) for 12 h at 4 °C. The mixture was finally washed and re-dispersed in PBS for future use.

Fabrication of the cathodic microfluidic PEC biosensor

As shown in Fig. 2B and C, 10 μL of EDC/NHS solution (1 × 10^{-2} mol L^{-1}/2 × 10^{-3} mol L^{-1}) was injected into the p–n AgI/Bi$_2$Ga$_4$O$_9$ WE (from inlet 1) to activate –COOH for 30 min at room temperature. Then, 8 μL of BSA (1 wt%) (from inlet 2) was injected to block the nonspecific binding sites to make sure that the 20 μL of Ab$_1$ (10 μg mL^{-1}) is well captured by the p–n AgI/Bi$_2$Ga$_4$O$_9$ after injection from inlet 3 to incubate for 60 min at 37 °C. After cleaning, 20 μL of CYFRA 21-1 antigen (from inlet 4) was injected for incubating. Finally, 20 μL of SOD@hMnO$_2$–Ab$_2$ (from inlet 5) was injected to fabricate the signal amplification immunocomplex to incubate for 60 min at 37 °C. All cleaning procedures were performed using PBS buffer solution with pH 7.0 to remove unabsorbed biomolecules after each modification step, which was injected at the injection port itself and outflowed through the outlet. All the cathodic photocurrent responses were determined in the wavelength range of the stimulation resource LED (Fig. S1, ESI†).

Results and discussion

Characterization of p–n AgI/Bi$_2$Ga$_4$O$_9$ and hMnO$_2$

The crystal structure of Bi$_2$Ga$_4$O$_9$ is characterized by X-ray diffraction (XRD). As shown in Fig. 3A, the diffraction peaks of the sample are well indexed to orthorhombic Bi$_2$Ga$_4$O$_9$ (JCPDS PDF# 76-2240), and the high purity of Bi$_2$Ga$_4$O$_9$ is observed from the absence of the characteristic peaks of impurities. Fig. 3B and C show the scanning electron microscopy (SEM) image of Bi$_2$Ga$_4$O$_9$ with a nanoplates assembled flower structure, which could provide a large orderly specific surface area to improve signal stability and reproducibility. As shown

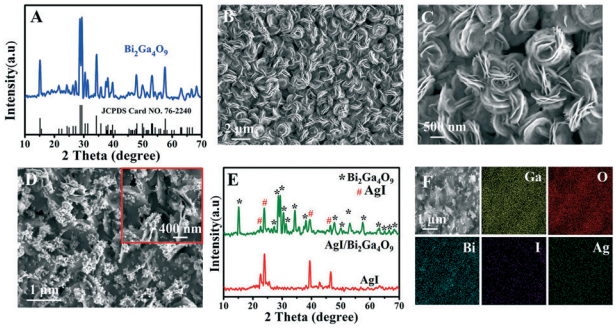

Fig. 3 The XRD pattern of (A) Bi$_2$Ga$_4$O$_9$; SEM images of (B) and (C) Bi$_2$Ga$_4$O$_9$; an SEM image of (D) AgI/Bi$_2$Ga$_4$O$_9$; XRD patterns of (E) AgI and AgI/Bi$_2$Ga$_4$O$_9$; and SEM elemental mapping of (F) AgI/Bi$_2$Ga$_4$O$_9$.

in Fig. 3D, the morphology and size of Bi$_2$Ga$_4$O$_9$ remains almost unchanged after growing AgI on the surface of Bi$_2$Ga$_4$O$_9$, whereas AgI with small nanoparticles is clearly viewed on the surface of Bi$_2$Ga$_4$O$_9$ (inset Fig. 3D). Meanwhile, Fig. 3E shows the XRD diffraction patterns of AgI and AgI/Bi$_2$Ga$_4$O$_9$ composites, which demonstrates that AgI could load on the surface of Bi$_2$Ga$_4$O$_9$, however, this does not influence the crystal structure of Bi$_2$Ga$_4$O$_9$. Moreover, the elemental distribution mapping in Fig. 3F presents the Ga, O, Bi, I and Ag elemental composition of AgI/Bi$_2$Ga$_4$O$_9$, further indicating the successful synthesis of the AgI/Bi$_2$Ga$_4$O$_9$ composites.

XPS is provided to identify the surface chemical states of the AgI/Bi$_2$Ga$_4$O$_9$ composites. As revealed in Fig. 4A, the main peaks of the XPS survey spectrum are observed to be the Bi, Ga, O, Ag and I elements, which fits well with the elemental mapping results. The high-resolution spectrum of Ag 3d and I 3d reveals two main peaks, respectively (inset Fig. 4A). As shown in Fig. 4B, two main peaks at 156.6 eV and 161.8 eV are assigned to Bi 4f$_{7/2}$ and Bi 4f$_{5/2}$, respectively, suggesting the existence of Bi^{3+}. Fig. 4C shows that the high-resolution spectrum of Ga 2p$_{3/2}$ and Ga 2p$_{1/2}$ have peaks at 1114.9 eV and 1141.7 eV, respectively, which revealed Ga 2p. The O 1s

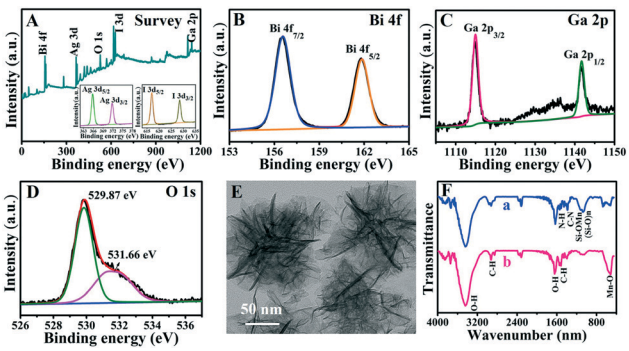

Fig. 4 XPS spectrum of (A) the AgI/Bi$_2$Ga$_4$O$_9$ composite (insets: XPS spectra of Ag 3d and I 3d); XPS spectrum of (B) Bi 4f; XPS spectrum of (C) Ga 2p; XPS spectrum of (D) O 1s; a TEM image of (E) hMnO$_2$; and FT-IR spectra of (F) hMnO$_2$ (curve b) and the amine functionalization of hMnO$_2$ (curve a).

peaks at 529.87 eV and 531.66 eV are ascribed to the surface hydroxyl groups and lattice oxygen (Bi–O or Ga–O),[30] respectively in Fig. 4D. The results exhibit the successful existence of AgI and $Bi_2Ga_4O_9$ in AgI/$Bi_2Ga_4O_9$.

For a comparative study, the UV-vis diffuse reflectance spectra (Fig. S2, ESI†) exhibit that the pure $Bi_2Ga_4O_9$ possesses an absorption wavelength range under 430 nm, which is attributed to the moderate band gap (~2.9 eV). On the other hand, the absorption of p–n AgI/$Bi_2Ga_4O_9$ undergoes a significant redshift, but between $Bi_2Ga_4O_9$ and AgI, which is expected. Obviously, after modification with AgI, the p–n AgI/$Bi_2Ga_4O_9$ could increase visible-light harvesting, which generates the greatest photoinduced charge separation and transfer under visible-light irradiation.

The crystallization of MnO_2 is characterized using XRD, and the result is exhibited in Fig. S3 (ESI†). Distinct diffraction peaks are recorded at 2θ = 12.18, 24.27, 36.53, and 65.75, which correspond to the (001), (002), (100), and (110) planes of birnessite-type MnO_2, respectively. The morphology and structure of MnO_2 is confirmed by the TEM image in Fig. 4E. MnO_2 has a honeycomb-like ($hMnO_2$) structure with a large surface with a uniform size of about 150 nm that was formed by the self-assembly of MnO_2 nanoplatelets. Moreover, the Fourier transform infrared (FT-IR) spectra are presented to demonstrate the successful amine functionalization of $hMnO_2$ in Fig. 4F. After the amination reaction (curve a), compared with the before amination reaction (curve b) the absorption peaks related to the Mn–O stretching vibration at 522.4 cm^{-1} and C–H bending vibration at 1518.2 cm^{-1} decrease, while additional absorption bands at 1052.6, 1126.3, 1388.9, and 1556.6 cm^{-1} appear, which are attributed to the stretching mode of the (Si–O)n, Si–OMn, C–N, and N–H, respectively, which suggests the successful amine functionalization of $hMnO_2$.

The increased electroactive surface area of p–n AgI/$Bi_2Ga_4O_9$

It is essential to evaluate the electro-active surface area of AgI/$Bi_2Ga_4O_9$, which can increase the loading of immune molecules on the sensing interface. To compare, the AgI/$Bi_2Ga_4O_9$ WE and pure WE are expressed by cyclic voltammetry (CV) employing a redox probe of $[Fe(CN)_6]^{4-/3-}$ solution. All analysis is based on the commonly used Randles–Sevcik equation:

$$I_p = 2.69 \times 10^5 A D^{1/2} n^{3/2} v^{1/2} c$$

where the I_p varies with the peak reduction current at different scan speeds, A is the electroactive surface area (cm^2) according to the decorated WE area, D is identified to be 6.70 ± 0.02 × 10^{-6} cm^2 s^{-1}, which represents the diffusion coefficient of $[Fe(CN)_6]^{4-/3-}$, n is 1 in this system, which represents the number of electrons transferred in the oxidation–reduction reaction, c is concentration of the $K_3Fe(CN)_6$ (5 × 10^{-3} mol L^{-1}), and v is CV scanning rate (V s^{-1}). Under different scan rates (Fig. 5A and S4A†), the regression equations of

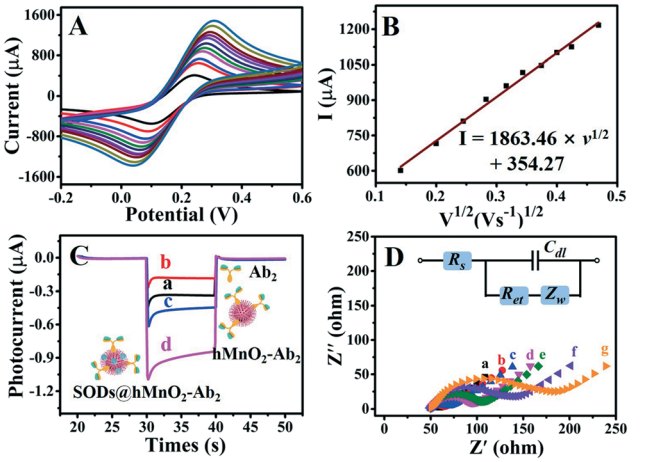

Fig. 5 CV detection of (A) AgI/$Bi_2Ga_4O_9$ WE in $[Fe(CN)_6]^{4-/3-}$ solution; the linear relationship between the peak reduction current I and $v^{1/2}$ of (B) AgI/$Bi_2Ga_4O_9$; the PEC performances of Ab_2 (curve b), $hMnO_2$–Ab_2 (curve c), and SOD@$hMnO_2$–Ab_2 (curve d) incubated on the CYFRA 21-1 antigen (curve a) modified WE (C); and EIS characterization of the stepwise proposed biosensor (D).

AgI/$Bi_2Ga_4O_9$ WE (Fig. 5B) and pure WE (Fig. S4B†) are acquired as I = 1863.46 × $v^{1/2}$ + 354.27 (R^2 = 0.992) and I = 796.5 × $v^{1/2}$ + 105.81 (R^2 = 0.984), respectively. Accordingly, the effective electrochemical active areas are obtained as 0.54 cm^2 and 0.23 cm^2 by calculation, respectively, suggesting the increased active surface area after modifying the p–n AgI/$Bi_2Ga_4O_9$ composites.

The excellent PEC performance of SOD@$hMnO_2$–Ab_2

To demonstrate that SOD@$hMnO_2$–Ab_2 could enhance the cathodic photocurrent response, the photocurrent–time curves of the prepared immunosensor are performed. As shown in Fig. 5C, the cathodic photocurrent decreases after incubating Ab_2 (curve b) with the CYFRA 21-1 antigen (curve a) modified p–n AgI/$Bi_2Ga_4O_9$ WE. Nevertheless, the cathodic photocurrent increases when $hMnO_2$–Ab_2 (curve c) is incubated on the CYFRA 21-1 antigen modified p–n AgI/$Bi_2Ga_4O_9$ WE. Interestingly, the cathodic photocurrent increases by about double after incubating with SOD@$hMnO_2$–Ab_2 (curve d) compared with $hMnO_2$–Ab_2 (curve c), indicating that it could be chosen as the signal amplification label.

Electrochemical impedance spectroscopy (EIS) of the biosensor

The different interface properties of the modified electrodes are characterized by EIS for the fabrication process of the biosensor. As shown in Fig. 5D, the electron-transfer resistance (R_{et}) increases gradually after modifying $Bi_2Ga_4O_9$ (curve b) and AgI (curve c) in sequence compared with bare WE (curve a). However, the relatively large value of R_{et} appears when modified with Ab_1 (curve d), due to the high steric hindrance and insulating property of the protein molecules. Afterwards, the R_{et} value is further increased step by step after modifying

with BSA (curve e), the target CYFRA 21-1 antigen (curve f), and the SOD@hMnO$_2$–Ab$_2$ (curve g) label for signal amplification layer by layer, suggesting that the biosensor is prepared successfully.

Discussion of the possible signal amplification mechanism

Mott–Schottky (M–S) measurements are conducted to fully understand the photocatalytic activity of the as-synthesized AgI/$Bi_2Ga_4O_9$ composites. The flat-band potential of $Bi_2Ga_4O_9$ and AgI is determined by M–S plots at −0.92 V and −0.88 V (Fig. S5, ESI†) *versus* the Ag/AgCl electrode, respectively, whose conduction band potential (ECB) is equivalent to −0.72 V and −0.68 V *versus* the normal hydrogen electrode (NHE).[31,32] Besides, UV-vis diffuse reflectance spectra of $Bi_2Ga_4O_9$ and AgI present a band gap (E_g) at 2.91 eV and 2.59 eV (Fig. S6, ESI†), respectively. Then, the valence band potential (EVB) of $Bi_2Ga_4O_9$ and AgI is 2.23 V and 1.87 V, respectively, which could be estimated *via* the following equation:

$$E_{VB} = E_g + E_{CB}$$

Fig. 6 shows the junction of AgI and $Bi_2Ga_4O_9$ under visible light irradiation. When p-type AgI contacts with n-type $Bi_2Ga_4O_9$ by an electrostatic self-assembly process, a built-in electric field is created at the interface of the p–n junction. Both AgI eqn (1) and $Bi_2Ga_4O_9$ eqn (2) can absorb visible photons to produce photogenerated electrons (e^-) and holes (h^+) under visible light irradiation. Then, driven by an internal electric field, the photogenerated e^- in the CB of AgI can be transferred directly to the CB of $Bi_2Ga_4O_9$ to dissolve O_2 to generate $^{\bullet}O_2^-$, while the h^+ photogenerated by $Bi_2Ga_4O_9$ in the VB is transferred to the VB of AgI, which enhances the efficient separation of e^-/h^+ pairs. Furthermore, the cathodic photocurrent density of p–n AgI/$Bi_2Ga_4O_9$ is much higher than that of pure AgI and $Bi_2Ga_4O_9$, which also proves the efficient separation of e^-/h^+ pairs (Fig. S7, ESI†).

For a better understanding of the signal amplification mechanism, a detailed possible illustration is as follows: (1) the e^- of $Bi_2Ga_4O_9$ in the CB can be captured by dissolved O_2 to generate $^{\bullet}O_2^-$ eqn (3). (2) Then, the $^{\bullet}O_2^-$ could be disproportionated into molecular O_2 and H_2O_2 by SOD on the label of SOD@hMnO$_2$–Ab$_2$ eqn (4). (3) More interestingly, the generated H_2O_2 could be degraded by MnO_2 to generate O_2 and H_2O eqn (5). In this way, the generated O_2 increases the content of dissolved O_2 trapped by more e^- in return, which obtains greatly amplified signals by efficient separation of e^-/h^+ pairs and consequently enhances the photocurrent conversion efficiency. To compare the effects of O_2-enhancement, the fabricated biosensor is detected in N_2-satuated Tris-HCl solution. However, the biosensor can hardly generate PEC signals in the N_2-saturated Tris-HCl solution (Fig. S8, ESI†).

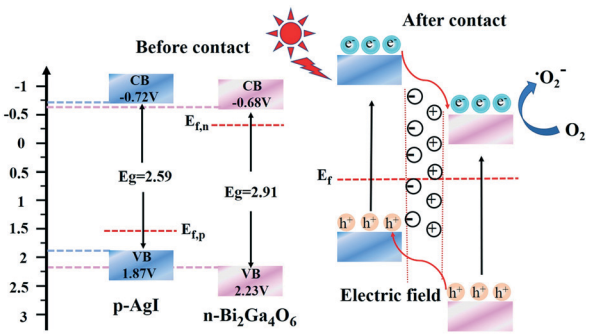

Fig. 6 A possible mechanism for boosting the efficient separation of e^-/h^+ pairs *via* the p–n AgI/$Bi_2Ga_4O_9$ junction under visible light irradiation.

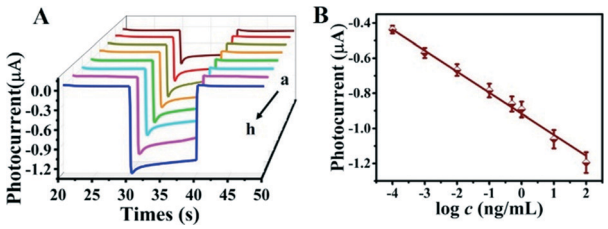

Fig. 7 Cathodic photocurrent intensity–time curves (A) with different concentrations from 0.1 pg mL^{-1} to 100 ng mL^{-1} obtained in 200 μL of Tris-HCl (0.1 M) in a microfluidic chip. The corresponding linear calibration curve for CYFRA 21-1 (B).

$$AgI + h\nu \rightarrow AgI\ (e^- + h^+) \quad (1)$$

$$Bi_2Ga_4O_9 + h\nu \rightarrow Bi_2Ga_4O_9\ (e^- + h^+) \quad (2)$$

$$e^- + O_2 \rightarrow {}^{\bullet}O_2^- \quad (3)$$

$$2{}^{\bullet}O_2^- + 2H^+ \xrightarrow{SOD} O_2 + H_2O_2 \quad (4)$$

$$H_2O_2 \xrightarrow{MnO_2} O_2 + H_2O \quad (5)$$

Analytical performance of the microfluidic cathodic PEC biosensor toward CYFRA 21-1

By coupling with the p–n AgI/$Bi_2Ga_4O_9$ as the platform and SOD@hMnO$_2$–Ab$_2$ as the signal amplification label, the detection of the CYFRA 21-1 standard was investigated in terms of the calibration relationship between cathodic photocurrent intensity under optimized experimental conditions (Fig. S9, ESI†). As exhibited in Fig. 7A, the cathodic photocurrent intensity of the biosensors increased with increasing the concentration of CYFRA 21-1 from 0.1 pg mL^{-1} to 100 ng mL^{-1}. The linear regression could be fitted to y (μA) = −0.9163 − 0.1199 × log $c_{\text{CYFRA 21-1}}$ ($c_{\text{CYFRA 21-1}}$ = ng mL^{-1}), R^2 = 0.995 (Fig. 7B) and the limit of detection (LOD) is estimated to be 0.026 pg mL^{-1} (S/N = 3). Besides, by comparing with previous reports (Table S1, ESI†), this proposed PEC biosensor presented a lower limit of detection and a wide linear range detection.

Table 1 Analytical recovery data of CYFRA 21-1 in human serum samples

Sample	Spiked concentration (ng mL^{-1})	Found concentration (ng mL^{-1})	RSD (n = 5, %)	Recovery (%)
1	0.01	0.124	2.67	95.20
	0.1	0.227	2.27	103.2
	1.0	1.09	3.52	97.30
	10	10.32	1.15	101.9

Analysis of human serum specimens

On the basis of the satisfactory specificity, reproducibility and stability (Fig. S10, ESI†) of the cathodic PEC biosensor, standard samples with different concentrations of CYFRA 21-1 (0.01 ng mL^{-1}, 0.1 ng mL^{-1}, 1.0 ng mL^{-1}, and 10 ng mL^{-1}) mixed with normal human serum were detected by a standard addition method to demonstrate the practicability and accuracy of the prepared cathodic PEC biosensor. The results exhibited that the average recoveries of the biosensor were from 95.2% to 103.2% with the RSD from 1.15% to 3.52% in Table 1, indicating the great potential of practicability of the developed biosensor.

Conclusions

In summary, a microfluidic cathodic PEC biosensor strategy is successfully proposed as a highly efficient signal amplification technique for biomarker detection. The p–n junction of AgI/$Bi_2Ga_4O_9$ possessed a strong internal electric field, which could improve the separation and transfer of photogenerated charge carriers and facilitate the generation of $^{\bullet}O_2^-$. Furthermore, AgI/$Bi_2Ga_4O_9$ with a high surface area and stable sensing platform could load more Ab_1. Then, $^{\bullet}O_2^-$ could be catalyzed to produce O_2 and H_2O_2 by SOD. Besides, the generated H_2O_2 could be further degraded by $hMnO_2$ to generate H_2O and O_2; O_2 as the electron acceptor could consume electrons in return, resulting in the further facilitation of the separation of e^-/h^+ pairs. Therefore, the amplifying signal is produced mainly by eliminating $^{\bullet}O_2^-$ and producing the electron acceptor of dissolved O_2. More importantly, the cathodic PEC immunosensor in the microfluidic chip with the advantages of rapid detection, high selectivity, and cost-effectiveness can be applied in human serum samples for detecting CYFRA 21-1. Hopefully, in the near future, new devices can be further integrated with advanced materials and microfabrication for other applications, such as detection of other tumor markers and cancer cells, or disease diagnostics and clinical analysis.

Author contributions

Jinhui Feng: conceptualization, methodology, writing – original draft. Tingting Wu and Qian Cheng: methodology and data analysis. Hongmin Ma and Xueying Wang: formal analysis and data curation. Jin Yong Lee: investigation. Xiang Ren: writing – review and editing. Qin Wei: validation and funding acquisition. Huangxian Ju: supervision and funding acquisition.

Conflicts of interest

There are no conflicts of interest to be declared by the authors.

Acknowledgements

This study was supported by the National Key Scientific Instrument and Equipment Development Project of China (No. 21627809), National Natural Science Foundation of China (No. 21777056), Special Foundation for Taishan Scholar Professorship of Shandong Province, Jinan Scientific Research Leader Workshop Project (2018GXRC024, 2018GXRC021), and the Innovation Team Project of Colleges and Universities in Jinan (No.2019GXRC027).

References

1 N. Singh, P. Rai, M. A. Ali, R. Kumar, A. Sharma, B. D. Malhotra and R. John, *J. Mater. Chem. B*, 2019, **7**, 3826–3839.
2 R. Gao, Z. Lv, Y. Mao, L. Yu, X. Bi, S. Xu, J. Cui and Y. Wu, *ACS Sens.*, 2019, **4**, 938–943.
3 J. Shu and D. Tang, *Anal. Chem.*, 2020, **92**, 363–377.
4 R. Yang, F. Li, W. Zhang, W. Shen, D. Yang, Z. Bian and H. Cui, *Anal. Chem.*, 2019, **91**, 13006–13013.
5 L. Ni, R. Shaik, R. Xu, G. Zhang and J. Zhe, *ACS Sens.*, 2020, **5**, 527–534.
6 J. Feng, Y. Qian, Q. Cheng, Y. Ma, D. Wu, H. Ma, X. Ren, X. Wang and Q. Wei, *Biosens. Bioelectron.*, 2020, **168**, 112503.
7 S. Yu, L. Mei, Y. Xu, T. Xue, G. Fan, D. Han, G. Chen and W. Zhao, *Anal. Chem.*, 2019, **91**, 3800–3804.
8 H. Zhang, Y. Yu, L. Zhang and S. Dong, *Angew. Chem., Int. Ed.*, 2018, **57**, 1547–1551.
9 F. A. L. Laskowski, M. R. Nellist, J. Qiu and S. W. Boettcher, *J. Am. Chem. Soc.*, 2019, **141**, 1394–1405.
10 W. Xu, J. Jia, T. Wang, C. Li, B. He, J. Zong, Y. Wang, H. Fan, H. Xu, Y. Feng and H. Chen, *Angew. Chem., Int. Ed.*, 2020, **59**, 22246–22251.
11 M. Zhang, J. Wang, H. Xue, J. Zhang, S. Peng, X. Han, Y. Deng and W. Hu, *Angew. Chem., Int. Ed.*, 2020, **57**, 18463–18467.
12 M. A. Lumley, A. Radmilovic, Y. J. Jang, A. E. Lindberg and K. S. Choi, *J. Am. Chem. Soc.*, 2019, **141**, 18358–18369.
13 J. Hua, S. Zhang, X. Li, K. Yun and F. Yu, *ChemElectroChem*, 2018, **5**, 3198–3205.
14 Y. Dong, Y. Chen, P. Jiang, G. Wang and C. Zhang, *Chem. – Asian J.*, 2015, **10**, 1660–1667.
15 W. Zhao, B. Dai, F. Zhu, X. Tu, J. Xu, L. Zhang, S. Li, D. Y. C. Leung and C. Sun, *Appl. Catal., B*, 2018, **229**, 171–180.

16 C. Zhou, C. Lai, P. Xu, G. Zeng, D. Huang, C. Zhang, M. Cheng, L. Hu, J. Wan and Y. Liu, *ACS Sustainable Chem. Eng.*, 2018, **6**, 4174–4184.
17 Y. Zhu, Z. Xu, K. Yan, H. Zhao and J. Zhang, *ACS Appl. Mater. Interfaces*, 2017, **9**, 40452–40460.
18 T. Liu, B. Liu, L. Yang, X. Ma, H. Li, S. Yin, T. Sato, T. Sekino and Y. Wang, *Appl. Catal., B*, 2017, **204**, 593–601.
19 F. Chen, Q. Yang, J. Sun, F. Yao, S. Wang, Y. Wang, X. Wang, X. Li, C. Niu, D. Wang and G. Zeng, *ACS Appl. Mater. Interfaces*, 2016, **8**, 32887–32900.
20 L. Zhang, C. Hu and H. Ji, *Appl. Catal., B*, 2017, **205**, 34–41.
21 Z. Lian, M. Sakamoto, J. J. Vequizo, C. K. Ranasinghe, A. Yamakata, T. Nagai, K. Kimoto, Y. Kobayashi, N. Tamai and T. Teranishi, *J. Am. Chem. Soc.*, 2018, **141**, 2446–2450.
22 K. Das, D. Majhi, Y. P. Bhoi and B. G. Mishra, *Chem. Eng. J.*, 2019, **362**, 588–599.
23 Y. Bai, Y. Zhou, J. Zhang, X. Chen, Y. Zhang, J. Liu, J. Wang, F. Wang, C. Chen, C. Li, R. Li and C. Li, *ACS Catal.*, 2019, **9**, 3242–3252.
24 K. S. Chaturvedi, C. S. Hung, D. E. Giblin, S. Urushidani and J. P. Henderson, *ACS Chem. Biol.*, 2013, **9**, 551–561.
25 K. Barnese, Y. Sheng, T. A. Stich, E. B. Gralla, R. D. Britt, D. E. Cabelli and J. S. Valentine, *J. Am. Chem. Soc.*, 2010, **132**, 12525–12527.
26 H. Fan, G. Yan, Z. Zhao, X. Hu, W. Zhang, H. Liu, X. Fu, T. Fu, X. Zhang and W. Tan, *Angew. Chem., Int. Ed.*, 2016, **55**, 5477–5482.
27 P. A. Ma, B. Ding, P. Zheng, F. Jiang and J. Lin, *Angew. Chem., Int. Ed.*, 2020, **59**, 16381–16384.
28 J. Liu, W. Lu, Q. Zhong, X. Jin and Z. Wang, *Mol. Catal.*, 2017, **433**, 354–362.
29 J. Liu, X. Zhang, Q. Zhong, J. Li, H. Wu, B. Zhang, L. Jin, H. Tao and B. Liu, *J. Mater. Chem. A*, 2020, **8**, 4083–4090.
30 X. Li, W. Zhang, J. Li, G. Jiang, Y. Zhou, S. Lee and F. Dong, *Appl. Catal., B*, 2019, **241**, 187–195.
31 Q. Wang, X. Shi, E. Liu, J. Xu, J. C. Crittenden, Y. Zhang and Y. Cong, *Ind. Eng. Chem. Res.*, 2016, **55**, 4897–4904.
32 Q. Xu, B. Zhu, B. Cheng, J. Yu, M. Zhou and W. Ho, *Appl. Catal., B*, 2019, **255**, 117770.